



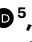
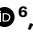
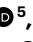





Reconciling disagreement on global river flood changes in a warming climate

Received: 30 December 2021

Accepted: 21 October 2022

Published online: 28 November 2022

 Check for updates

Shulei Zhang ¹✉, Liming Zhou ², Lu Zhang ^{3,4}, Yuting Yang ⁵,
Zhongwang Wei ¹, Sha Zhou ⁶, Dawen Yang ⁵, Xiaofan Yang ⁶,
Xiuchen Wu ⁶, Yongqiang Zhang ⁷, Xiaoyan Li ⁶ & Yongjiu Dai ¹✉

An intensified hydrological cycle with global warming is expected to increase the intensity and frequency of extreme precipitation events. However, whether and to what extent the enhanced extreme precipitation translates into changes in river floods remains controversial. Here we demonstrate that previously reported unapparent or even negative responses of river flood discharge (defined as annual maximum discharge) to extreme precipitation increases are largely caused by mixing the signals of floods with different generating mechanisms. Stratifying by flood type, we show a positive response of rainstorm-induced floods to extreme precipitation increases. However, this response is almost entirely offset by concurrent decreases in snow-related floods, leading to an overall unapparent change in total global floods in both historical observations and future climate projections. Our findings highlight an increasing rainstorm-induced flood risk under warming and the importance of distinguishing flood-generating mechanisms in assessing flood changes and associated social-economic and environmental risks.

Global warming is the most widely recognized signature of anthropogenic climate change and has profoundly affected the Earth's hydrologic system and increased the risks of hydrometeorological natural hazards^{1,2}. Observational evidence and climate model projections consistently suggest widespread increases in the frequency and magnitude of extreme precipitation in response to warming-induced increases in atmospheric water-holding capacity^{3–6}, which is expected to intensify river flooding^{7,8}. However, direct assessments of historical floods do not always support this assertion: observations of historical floods show both increasing and decreasing trends at the regional scale with little systematic change globally^{9–17}, and the global patterns of flood–temperature scaling relationships remain controversial^{18–20}. The inconsistency in the relationship between extreme precipitation

and flooding with temperature highlights the challenge in predicting the risk of flooding and the consequent economic and social losses under future warming.

Conventionally, flood changes are often assessed without considering flood types throughout the entire study period and domain (quantified either by annual maximum approach^{12–15} or peaks-over-threshold approach^{9–11}). However, flooding is a complex physical process that involves interactions among hydrology, meteorology and land surface features, and can be triggered by multiple mechanisms^{21–25} (for example, intense rainfall, long-lasting and low-intensity rainfall, rain-on-snow and snow-melt). Even for the same catchment, the generating mechanism of floods may vary over time²². Assessments without considering

¹Southern Marine Science and Engineering Guangdong Laboratory (Zhuhai), School of Atmospheric Sciences, Sun Yat-sen University, Guangzhou, China.

²Department of Atmospheric and Environmental Sciences, University at Albany, State University of New York, Albany, NY, USA. ³State Key Laboratory of Water Resources and Hydropower Engineering Science, Wuhan University, Wuhan, China. ⁴CSIRO Land and Water, Black Mountain, Canberra, Australia.

⁵State Key Laboratory of Hydrosience and Engineering, Department of Hydraulic Engineering, Tsinghua University, Beijing, China. ⁶State Key Laboratory of Earth Surface Process and Resource Ecology, Faculty of Geographical Science, Beijing Normal University, Beijing, China. ⁷Key Laboratory of Water Cycle and Related Land Surface Processes, Institute of Geographical Sciences and Natural Resources Research, Chinese Academy of Sciences, Beijing, China. ✉e-mail: zhangshlei@mail.sysu.edu.cn; daiyj6@mail.sysu.edu.cn

flood types may mix the signals of changes in floods driven by different mechanisms, which could directly lead to erroneous conclusions regarding how flood changes with various driving factors (for example, storm, snowmelt, soil moisture, land cover change) under warming¹⁸.

To address this issue and advance a predictive understanding of flood changes under historical conditions and future warming, we first categorize a total of 246,170 annual maximum flood events (that is, events with annual maximum streamflow from 1950 to 2017) in 7,239 catchments globally over the past seven decades into different flood types (Supplementary Figs. 1–5). A classification algorithm is developed and applied to categorize flood events into four types. This algorithm consists of a decision tree that defines the dominant driving factors of each flood type and a statistical clustering algorithm that determines the classification thresholds (see Methods). The four flood types include (1) intense rainfall-induced maximum flood (IR-MF), (2) excessive soil moisture-induced maximum flood (ES-MF), (3) snowmelt-induced maximum flood (SM-MF) and (4) rain-on-snow-induced maximum flood (RS-MF). These event-based flood types are used to determine the dominant flood type for each catchment on the basis of which all catchments are stratified into four groups for long-term trend analysis. We then investigated the historical evolutions of different types of flood and their relationships with changes in extreme precipitation under warming. Using the latest climate projections from state-of-the-art climate models participating in the Coupled Model Intercomparison Project 6 (CMIP6), we lastly explored the translation of enhanced extreme precipitation under future warming to changes in floods by comparing their trends and the shifts in scaling relationships with temperature (Supplementary Fig. 6). The overall goal is to clarify and reconcile the disagreements on global river flood changes under a warming climate.

Classification of flood types

During the past decades, the annual maximum flood events show substantial disparities in flood type across catchments and the proportions of each flood type in individual catchments (Fig. 1a–d). IR-MFs, ES-MFs, SM-MFs and RS-MFs occurred in 93.5%, 92.4%, 56.8% and 77.8% of the 7,239 catchments, respectively. Over 94.3% of the catchments experienced multiple types of flood. For all the identified flood events, IR-MF, ES-MF, SM-MF and RS-MF accounted for 31.4%, 27.2%, 19.8% and 21.6%, respectively.

Different flood types exhibit diverse spatial patterns, with IR-MFs mainly occurring in low and mid latitudes of North America, southwestern Europe and most catchments in the Southern Hemisphere (Fig. 1a). The proportion of ES-MFs broadly follows that of IR-MFs, but a much higher proportion of ES-MFs was found in the tropics and western Europe (Fig. 1b). In contrast, high proportions of snow-related floods (SM-MFs and RS-MFs) were generally found in high latitudes and mountainous regions (for example, the Alps Mountains and the Rocky Mountains extending from eastern Alaska to the southwestern United States; Fig. 1c,d). These patterns are generally consistent with global/regional flood classifications conducted previously, especially in the United States and Europe^{24,25}, despite slight differences in the classification results between IR-MF and ES-MF due to different definitions of antecedent catchment wetness conditions²⁴. Additionally, the classified type of floods also aligned well with common understandings of the timing for each flood type, for example, snow-related floods mainly occurred in late winter and spring, while IR-MFs dominated in summer and autumn (Supplementary Fig. 7). We further divided the 7,239 catchments into four groups on the basis of their dominant flood type (that is, the flood type showing the highest proportion of occurrence; Fig. 1e), and the ratios of catchments dominated by IR-MFs, ES-MFs, SM-MFs and RS-MFs accounted for 34.9%, 22.7%, 21.8% and 20.6%, respectively.

Historical changes in different types of flood

We examined historical changes in flood magnitude (annual maximum streamflow) and extreme precipitation (annual maximum precipitation) during the period 1950–2017 in the 7,239 catchments. The spatially aggregated annual maximum floods (by calculating the time series of annual maximum streamflow at each catchment and then averaging the values across all catchments) showed a minor and non-significant trend ($0.10 \text{ mm d}^{-1} \text{ decade}^{-1}$, $P = 0.11$) over the past 68 yr (Fig. 2a), despite a significant increasing trend in the aggregated annual maximum precipitation ($0.42 \text{ mm d}^{-1} \text{ decade}^{-1}$, $P < 0.01$). However, such results differ among individual flood types (Fig. 2d–g). Specifically, the aggregated IR-MFs showed a significant upward trend over the past decades at a rate of $0.21 \text{ mm d}^{-1} \text{ decade}^{-1}$ ($P < 0.01$). Similarly, a positive trend was found for ES-MFs, with a non-significant rate of $0.07 \text{ mm d}^{-1} \text{ decade}^{-1}$ ($P = 0.13$). In contrast, SM-MFs and RS-MFs both experienced decreasing trends at a rate of $-0.12 \text{ mm d}^{-1} \text{ decade}^{-1}$ ($P < 0.01$) and $-0.11 \text{ mm d}^{-1} \text{ decade}^{-1}$ ($P = 0.13$), respectively. Evidently, the increasing trends in IR-MFs and ES-MFs have largely been offset by the concurrent decreasing trends in SM-MFs and RS-MFs, leading to an overall minor change in the annual maximum floods over the past 68 yr. The robustness of this finding is further confirmed by uncertainty analyses of the impacts of variations in flood classification thresholds and catchment samples on the aggregated trend analysis (Supplementary Texts 1 and 2).

We next investigated the trends in annual maximum flood and precipitation in individual catchments (Fig. 2b,c). Increased annual maximum precipitation was found in most of the catchments (70.1%), and this increase almost equally occurred in the four groups of catchments dominated by different types of flood (Fig. 2b). As for changes in floods, the number of catchments showing a positive change more or less equalled that showing a negative change (50.6% versus 49.4%). However, 64.5% (20.9%) of IR-MF dominated catchments and 60.8% (18.8%) of ES-MF dominated catchments showed significantly increased floods during the study period (Fig. 2c and Supplementary Fig. 8b). In comparison, only 32.6% (10.2%) and 43.2% (14.5%) of SM-MF and RS-MF dominated catchments exhibited significant increases in floods. In the catchments with increased extreme precipitation, the proportion of catchment agreeing on the direction of the positive change in floods and extreme precipitation is 72.3% (IR-MF), 65.5% (ES-MF), 34.5% (SM-MF) and 47.4% (RS-MF), respectively, for the four groups of catchments. This indicates that whether intensified extreme precipitation translates into an increase in flooding depends greatly on the dominant flood type (different flood-generating mechanisms) at the regional scale.

To further explore the relationship between changes in floods and extreme precipitation during the historical period, we compared the scaling curves of streamflow (Q) with air temperature (T) and precipitation (P), with T referred to as the Q - T and P - T scaling curve, respectively. A ‘hook’-like structure (or peak structure) has been widely reported for the scaling curve of P - T ^{6,26}, which features a peak point temperature ($T_{\text{peak-P}}$) at which the extreme percentile of daily P reaches its peak during a given period (Supplementary Fig. 6a). A similar structure and peak point temperature ($T_{\text{peak-Q}}$; Supplementary Fig. 6c) has also been found for the scaling curve of Q - T ^{7,19}. When comparing the peak point temperatures of the scaling curves ($T_{\text{peak-P}}$ and $T_{\text{peak-Q}}$) at the catchments, a good agreement between $T_{\text{peak-P}}$ and $T_{\text{peak-Q}}$ mainly appears in regions where floods are dominated by IR-MF and ES-MF, with a Pearson correlation coefficient (R) of 0.62 ($P < 0.01$) and 0.59 ($P < 0.01$) (Supplementary Fig. 9), respectively. Additionally, the correlation between $T_{\text{peak-P}}$ and $T_{\text{peak-Q}}$ increases with the proportions of these two flood types (Fig. 3c,d). For example, for catchments with proportion of IR-MF (or ES-MF) larger than 75%, the correlation coefficient is as high as 0.85 (or 0.82). Evidently, the Q - T relationship closely follows the P - T relationship, and the peak of Q is largely controlled by the peak of P in these catchments. In contrast, the correlations between $T_{\text{peak-P}}$ and $T_{\text{peak-Q}}$ are rather weak (and are

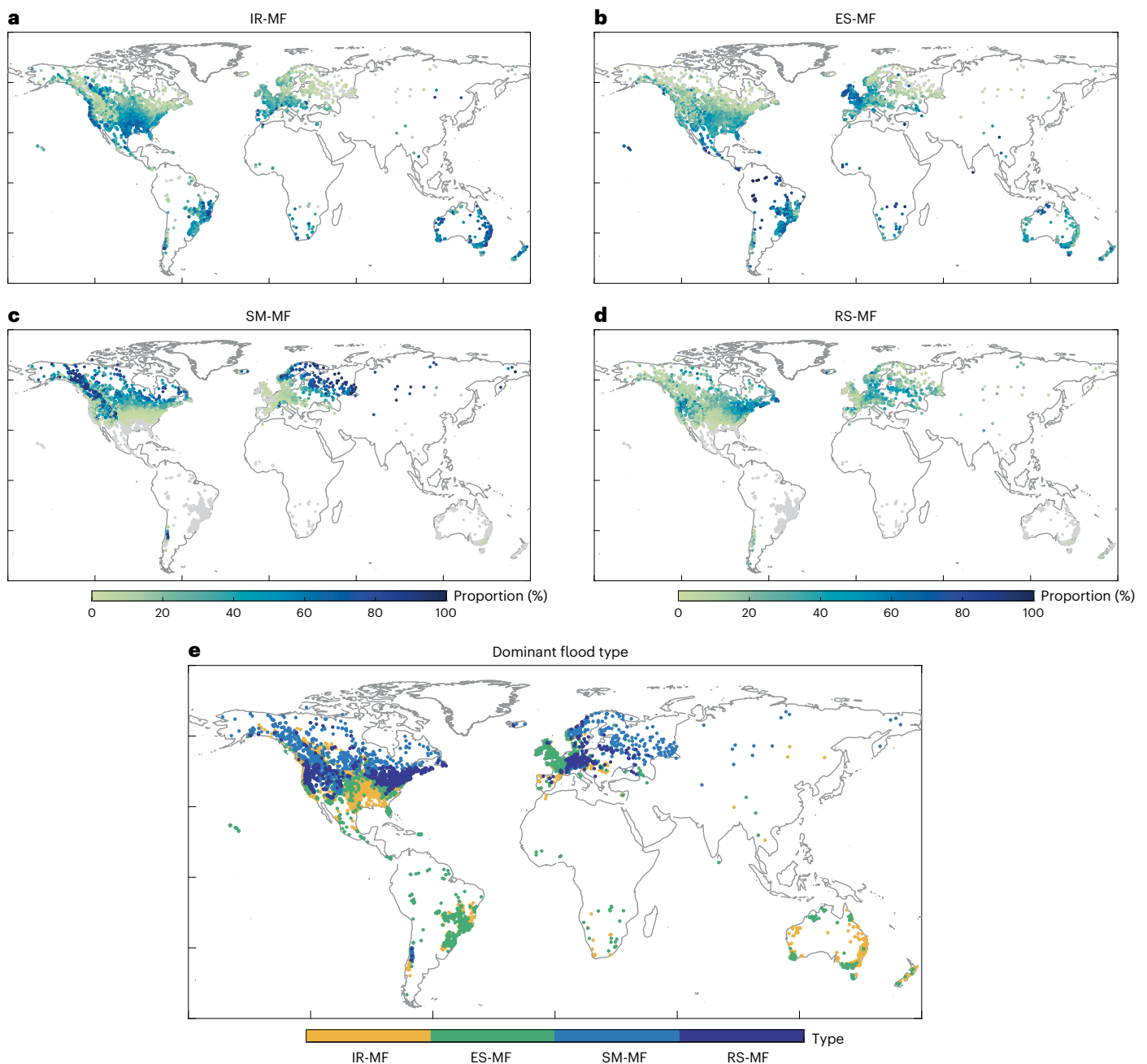


Fig. 1 | Classification of annual maximum flood events in the 7,239 catchments. a–d, Proportions of four types of flood event, IR-MF (a), ES-MF (b), SM-MF (c) and RS-MF (d), in individual catchments. The grey points represent

catchments with a zero proportion of a specific flood type. **e,** Spatial distribution of four groups of catchments classified on the basis of their dominant type (that is, the flood type showing the highest proportion of occurrence).

even negative) in catchments dominated by snowmelt-related floods (Fig. 3e,f and Supplementary Fig. 9), with $T_{\text{peak-Q}}$ generally concentrated in a relatively narrow range around 5°C (which should be the temperature at which the catchments experience substantial snowmelt²⁷) despite large variations in $T_{\text{peak-P}}$. In this case, it is easy to understand the inconsistency in changes of floods and extreme precipitation in these regions as the generation of floods is not necessarily related to extreme precipitation.

Flood changes under future warming

To explore changes in floods under future warming, we used outputs from 11 CMIP6 models from 1950 to 2100 (1950–2014 for historical simulations and 2015–2100 for future projections under the SSP585 and

SSP245 scenarios). First, model performance in reproducing floods and extreme precipitation was assessed by comparing with observations (Supplementary Text 3). Although the models capture flood dynamics less well than extreme precipitation at the catchment scale, the ensemble model outputs broadly capture the magnitudes of mean annual maximum Q (Supplementary Fig. 16), the direction of changes in annual maximum Q (Supplementary Fig. 17) and the outcomes of flood classification (Supplementary Fig. 18) on the basis of observations in validation catchments. Furthermore, the relationships between $T_{\text{peak-P}}$ and $T_{\text{peak-Q}}$ for the four groups of catchments dominated by different types of flood are similar between model outputs (Supplementary Fig. 19) and observations. These results indicate that the models are generally capable of capturing the observed key responses of floods

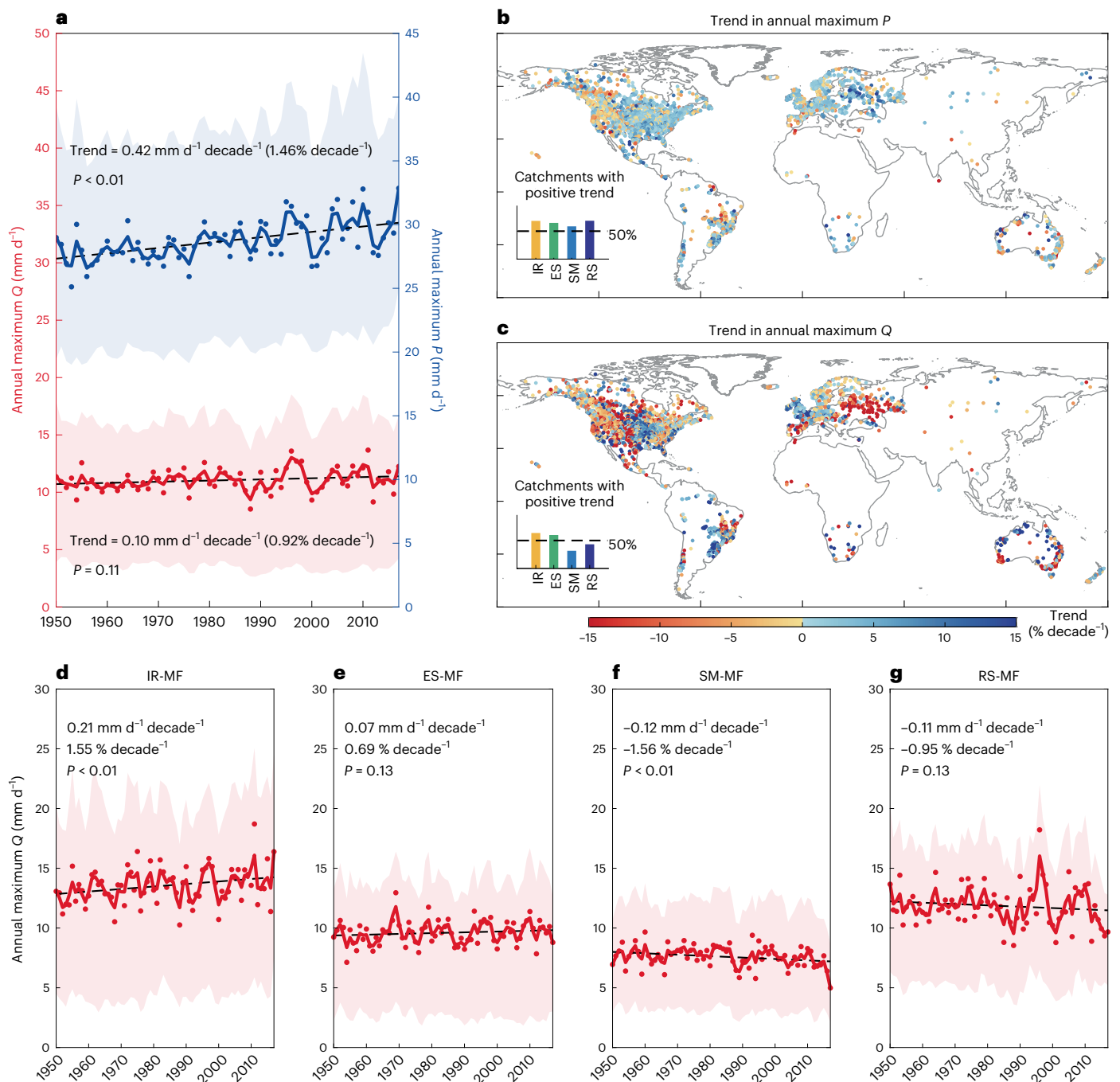


Fig. 2 | Changes in annual maximum flood and precipitation in the 7,239 catchments from 1950–2017. a, Time series of annual maximum precipitation and streamflow averaged over all catchments from 1950 to 2017. Shaded bands indicate the spatial variability among catchments (25th and 75th percentiles). Solid lines show the smoothed time-series data (three-year moving averages). Dashed lines represent the fitted trends estimated using linear regression with time as the dependent variable, with significance level (two-tailed Student's *t*-test) indicated. **b,c**, Spatial patterns of trends in annual maximum precipitation

(**b**) and flood (**c**) in individual catchments. Insert bars represent the proportions of catchments with positive trends (both significant and non-significant) in four groups of catchments, with the proportions of catchments showing significant trends provided in Supplementary Fig. 8a,b. **d–g**, Time series of annual maximum precipitation and flood averaged over four groups of catchments classified on the basis of the dominant flood type, IR-MF (**d**), ES-MF (**e**), SM-MF (**f**) and RS-MF (**g**). The shaded bands, solid lines and dashed lines are similarly defined as in **a**.

to climate change during the historical period and can thus be used to extrapolate these responses into the future.

Global changes in floods and extreme precipitation from the past to the future (under high-emission scenario SSP585) based on multi-model ensemble outputs are illustrated in Fig. 4. The upward trend in annual maximum precipitation observed in the historical

period would persist into the future across most parts of the globe at an average rate of 1.62% decade⁻¹. By contrast, the trend in floods exhibits mixed spatial patterns under future warming. Significant increases in floods are projected to occur in vast areas of mid and low latitudes (Fig. 4b) that are generally dominated by IR-MFs (Fig. 1a) and Extended Data Fig. 1a) and ES-MFs (Fig. 1b and Extended Data Fig. 1b). In Australia,

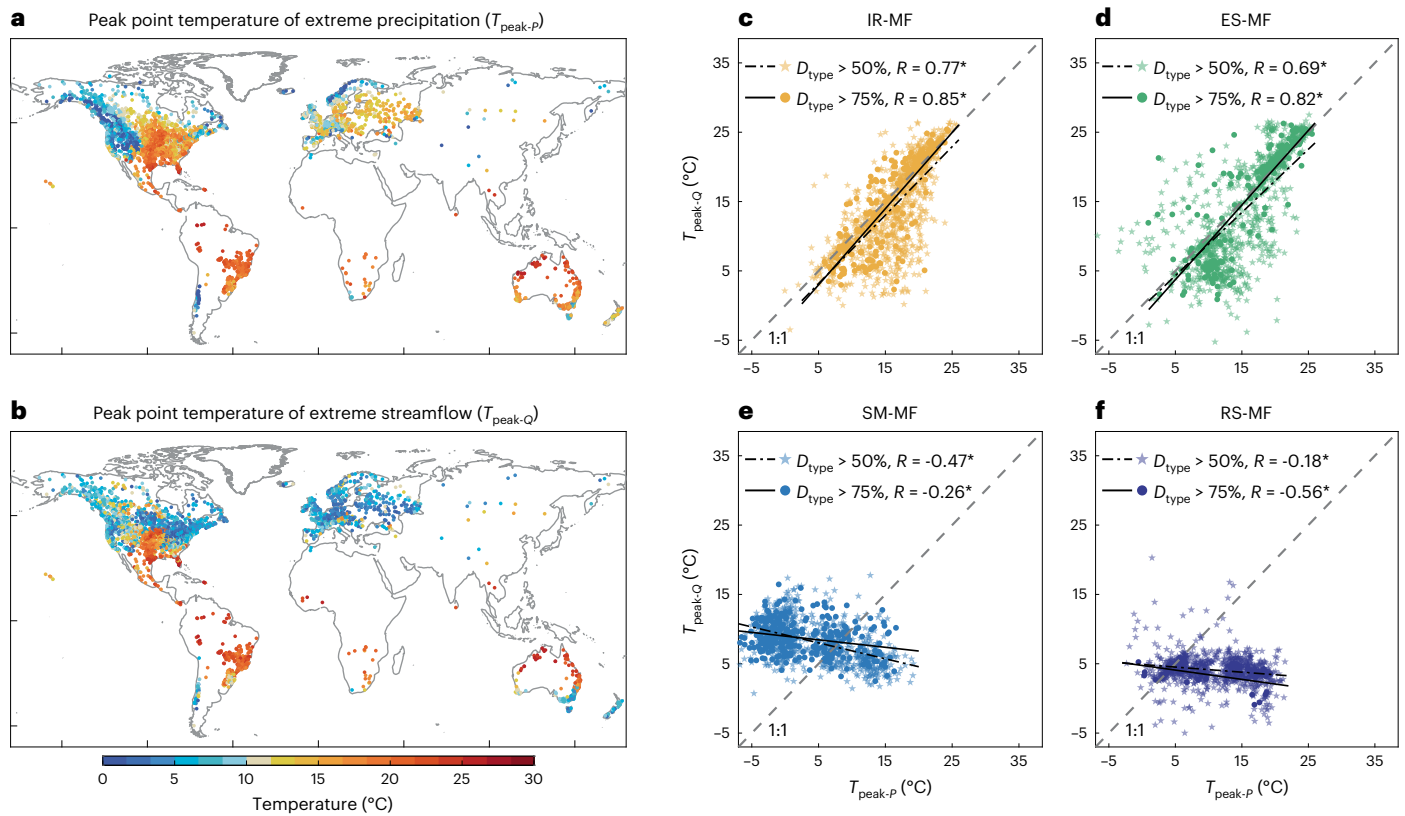


Fig. 3 | Comparison between the peak point temperatures of the P - T and Q - T scaling curves. a, b, Spatial patterns of the peak point temperature of the P - T scaling curve (a) and Q - T scaling curve (b), that is, $T_{\text{peak-P}}$ and $T_{\text{peak-Q}}$, in the 7,239 catchments. **c–f**, Comparison between $T_{\text{peak-P}}$ and $T_{\text{peak-Q}}$ for four groups of

catchments dominated by IR-MF (c), ES-MF (d), SM-MF (e) and RS-MF (f) with different proportions of dominant type (D_{type}). Pearson correlation coefficients (R), regression lines between $T_{\text{peak-P}}$ and $T_{\text{peak-Q}}$ and statistical significance ($*P < 0.01$) are shown.

the eastern United States, southern South America, East-South Asia and Africa, the relative increase in floods is even higher than that of extreme precipitation (Fig. 4c). However, at high latitudes (for example, majority of Europe and northern North America) and some mountainous regions (for example, the Rocky Mountains in North America) where SM-MF and RS-MF tend to dominate (Fig. 1c,d and Extended Data Fig. 1c,d), the projected floods show a decreasing trend over the same period (Fig. 4c). The concurrent positive (a trend of $2.01\% \text{ decade}^{-1}$ for IR-MFs and $1.52\% \text{ decade}^{-1}$ for ES-MFs) and negative (a trend of $-0.79\% \text{ decade}^{-1}$ for SM-MFs and $-0.25\% \text{ decade}^{-1}$ for RS-MFs) flood changes, when combined, result in a relatively small overall trend ($0.72\% \text{ decade}^{-1}$). Similar results have been found on the basis of model outputs under low-emission scenario (SSP245; Extended Data Fig. 2), demonstrating again that warming-induced increases in extreme precipitation do translate into increased floods over many regions except for areas where floods are primarily triggered by snowmelt.

We further investigated the shifts in P - T and Q - T scaling curves (quantified by the shifts in peak points of the curves) from the historical (1950–2014) to the future (2015–2100) periods (Fig. 5 and Supplementary Fig. 11). The P - T scaling curves show positive shift rates over most of the globe ($\sim 95\%$; Fig. 5a), with an average value of $4.9\% \text{ }^{\circ}\text{C}^{-1}$ under high-emission scenario (Fig. 5b), again indicating increasing extreme precipitation with rising temperature. At mid and low latitudes where IR-MFs and ES-MFs dominate, the shifts in Q - T scaling curves follow those of the P - T scaling curves over most regions (Fig. 5b,c), with $\sim 75\%$ of areas exhibiting a positive shift rate, which indicates rising streamflow extremes under warming (Fig. 5a). At high-latitude regions dominated by snow-related floods, the shift in Q - T scaling curves also exhibits a positive rate in more than 50% of the regions, while only $\sim 30\%$ of the

areas in these regions show a positive trend in streamflow extremes under warming (Fig. 5a), with an overall decreasing trend (Fig. 4f,g). We found that the positive (or high) shift rate therein does not indicate a large increase in floods under warming as it is mainly contributed by the small (or even negative) changes in $T_{\text{peak-Q}}$ (Extended Data Fig. 3) instead of increases in floods. The P - T and Q - T scaling curves and their peak points show substantial differences in these regions (Fig. 3e,f), and so do the shifts in the scaling curves. Evidently, one should be cautious when using the scaling relationships to quantify and/or compare the response of extreme precipitation and streamflow to warming in regions where floods are related to snow. It again underscores the importance of considering region-dependent flood generation mechanisms when assessing flood changes under climate change.

Discussion

Existing assessments of historical flood changes did not reveal an overwhelming flood increase in response to widespread increases in extreme precipitation induced by warming^{9–17}. However, our results clearly demonstrate that the relationship between changes in extreme precipitation and changes in floods under global warming, and the resulting flood risks would be largely misinterpreted without considering the flood types. Here we present evidence that warming-induced increased extreme precipitation did translate into increased river floods in regions where rainstorm-induced floods dominate (for example, southeastern United States, western Europe, south of South America; Fig. 2c), which is further supported by the consistency in the P - T and Q - T scaling relationships therein (Fig. 3c,d). This positive response of floods to extreme precipitation will persist into the future across these regions, with an accelerating trend in flooding as projected by

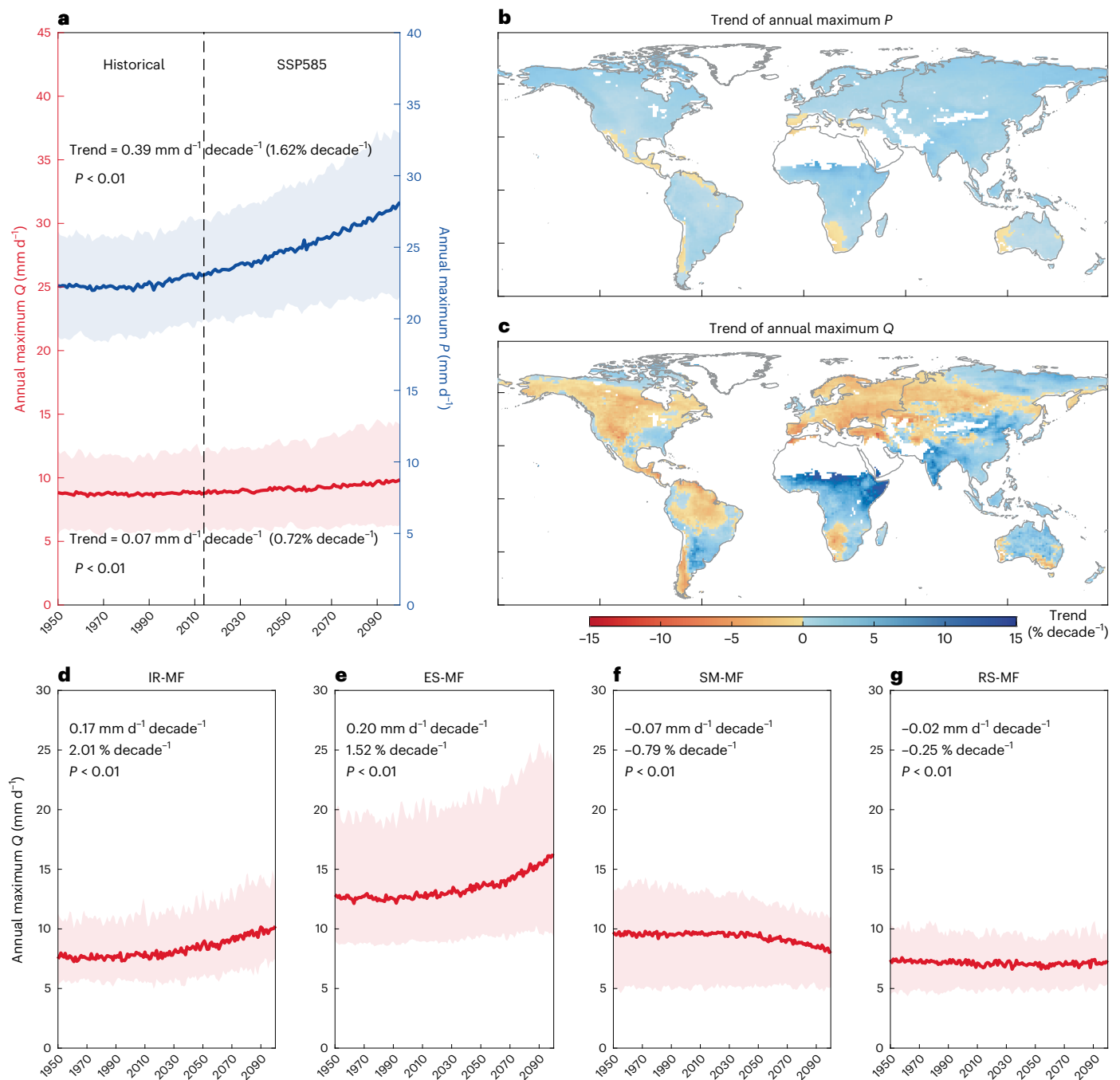


Fig. 4 | Changes in flood and extreme precipitation from the historical to the future period. a, Time series of annual maximum precipitation (P) and streamflow (Q) averaged over the global land area from the historical (1950–2014 under historical forcing) to the future (2015–2100 under the SSP585 scenario) period based on the outputs of 11 CMIP6 models. Shaded bands represent the variation by individual model. The trends were estimated on the basis of the ensemble mean of model outputs using linear regression, with significance level

(a two-tailed Student's t -test) indicated. **b,c**, Global patterns of the trends in annual maximum P (**b**) and Q (**c**) from 1950 to 2100. The whitespace represents dry lands with very limited run-off. **d–g**, Time series of annual maximum Q averaged over regions dominated by different flood types, IR-MF (**d**), ES-MF (**e**), SM-MF (**f**) and RS-MF (**g**). The shaded bands, solid lines and dashed lines are similarly defined as in **a**.

climate models (Fig. 4d,e), suggesting an increasing flood risk under future warming.

In contrast, regions dominated by snowmelt-related floods experienced opposite changes in floods and extreme precipitation during the historical period, that is, reduced floods with increasing extreme precipitation (Fig. 2f,g), which would offset the increasing trends of rainstorm-induced floods when lumping floods of different types

(Figs. 2a and 4a). As illustrated by the difference in their scaling relationships with temperature (Fig. 3e,f), the generation of snowmelt-related floods, which are greatly affected by variations in snow accumulations²⁸ and/or shortened snow duration²⁹ as the climate continues to warm, is not directly related to extreme precipitation. In this case, it would be misleading to extrapolate flood risks in the future on the basis of the changes in extreme precipitation (Figs. 4 and 5). However, it should also

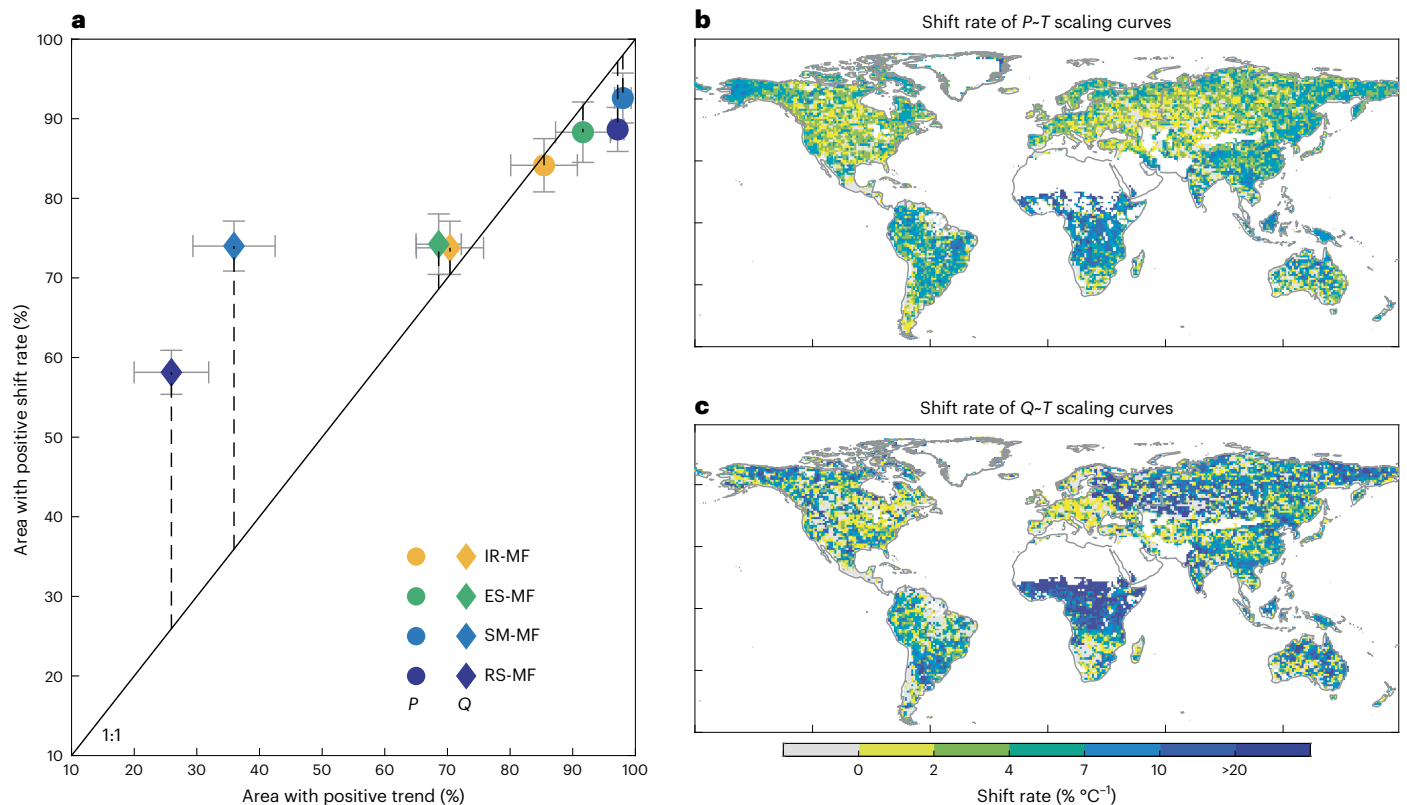


Fig. 5 | Changes in peak points of the P - T and Q - T scaling curves from the historical to the future period. **a, Comparison between the ratio of the area with positive trends in annual maximum P (Q) to the total area and the ratio of the area with positive shift rates of P - T (Q - T) scaling curves to the total area in four groups of regions dominated by different flood types based on the outputs of 11 CMIP6 models from the historical (1950–2014 under historical forcing) to the future**

(2015–2100 under SSP585 scenario) period. Error bars indicate the variations among 11 models (mean ± 1 s.d.). **b, c**, Global patterns of the shift rates of the P - T scaling curves (**b**) and Q - T scaling curves (**c**) from the historical to the future period (SSP585 scenario). The shift rates (% °C⁻¹) quantify the percentage shifts in scaling curves (that is, the changes in precipitation or streamflow extremes in the scaling curves).

be noted that a decrease in snowmelt-related flood magnitude (peak streamflow) does not necessarily lead to reduced flood risks in these regions. Studies reported that historically snow-dominated mountainous regions tend to shift from spring snowmelt-driven events towards more frequent rainstorm-dominated winter floods³⁰. The shifts in the timing of snowmelt also have major impacts on flood controls, water resources management and aquatic/riparian ecosystems³¹.

In addition to the contrasting changes between rainstorm-induced floods and snow-related floods, we also observe differences between changes in IR-MF and ES-MF, and between changes in SM-MF and RS-MF. Compared with IR-MF, ES-MF may be more susceptible to changes in soil moisture, especially antecedent soil moisture^{32,33}. Declines in soil moisture may partly offset the positive response of ES-MF to increased precipitation and therefore result in smaller increases in ES-MF³⁴. RS-MF exhibits a more complicated change pattern than the other three flood types as it involves both extreme precipitation and snowmelt process. Besides, studies found that changes in RS-MF under warming are also related to elevation that affects the development of snowpack³⁵. Snowmelt was estimated by a simple degree-day model in this study, this model probably introducing uncertainty in classifying these two types of snowmelt-related flood. A more accurate classification between SM-MF and RS-MF with higher-resolution snowmelt observations and/or more physically based snowmelt models would reduce the uncertainty. Furthermore, this study focused on annual peak flow, whereas literature has shown that climate change may have different impacts on floods of varying magnitudes¹⁸, which may differ in terms of flood-generating mechanisms. Future work on floods of different magnitudes using the framework of this study will

provide a more complete picture of the impact of climate change on flood risk.

In summary, the generation of floods is highly complex and involves nonlinear interactions among climate, landscape and the hydrological system^{19,21–25}. A better understanding of such interactions is a prerequisite for identifying/attributing the changing signals in flood records and forecasting future changes in flood risks in a changing climate. This study reconciles the previous controversial findings on global flood trends under warming by revealing diverse changing signals of floods with different generating mechanisms and their relationships with warming-induced increases in extreme precipitation. It highlights the importance of distinguishing flood types for understanding the effect of warming on the occurrence of hydrological extremes, and provides consequential information for flood risk assessment and policy interventions for water-related disaster management under a changing climate.

Online content

Any methods, additional references, Nature Portfolio reporting summaries, source data, extended data, supplementary information, acknowledgements, peer review information; details of author contributions and competing interests; and statements of data and code availability are available at <https://doi.org/10.1038/s41558-022-01539-7>.

References

- Allan, R. P. & Soden, B. J. Atmospheric warming and the amplification of precipitation extremes. *Science* **321**, 1481–1484 (2008).

2. Hirabayashi, Y. et al. Global flood risk under climate change. *Nat. Clim. Change* **3**, 816–821 (2013).
3. Lenderink, G. & Van Meijgaard, E. Increase in hourly precipitation extremes beyond expectations from temperature changes. *Nat. Geosci.* **1**, 511–514 (2008).
4. Trenberth, K. E., Dai, A., Rasmussen, R. & Parsons, D. The changing character of precipitation. *Bull. Am. Meteorol. Soc.* **84**, 1205–1217 (2003).
5. Fischer, E. M. & Knutti, R. Observed heavy precipitation increase confirms theory and early models. *Nat. Clim. Change* **6**, 986–991 (2016).
6. Prein, A. F. et al. The future intensification of hourly precipitation extremes. *Nat. Clim. Change* **7**, 48–52 (2017).
7. Yin, J. et al. Large increase in global storm runoff extremes driven by climate and anthropogenic changes. *Nat. Commun.* **9**, 4389 (2018).
8. Ali, H., Modi, P. & Mishra, V. Increased flood risk in Indian sub-continent under the warming climate. *Weather Clim. Extrem.* **25**, 100212 (2019).
9. Mallakpour, I. & Villarini, G. The changing nature of flooding across the central United States. *Nat. Clim. Change* **5**, 250–254 (2015).
10. Slater, L. J. & Villarini, G. Recent trends in U.S. flood risk. *Geophys. Res. Lett.* **43**, 12428–12436 (2016).
11. Archfield, S. A., Hirsch, R. M., Viglione, A. & Blöschl, G. Fragmented patterns of flood change across the United States. *Geophys. Res. Lett.* **43**, 10232–10239 (2016).
12. Zhang, X. S. et al. How streamflow has changed across Australia since the 1950s: evidence from the network of hydrologic reference stations. *Hydrol. Earth Syst. Sci.* **20**, 3947–3965 (2016).
13. Blöschl, G. et al. Changing climate both increases and decreases European river floods. *Nature* **573**, 108–111 (2019).
14. Do, H. X., Westra, S. & Leonard, M. A global-scale investigation of trends in annual maximum streamflow. *J. Hydrol.* **552**, 28–43 (2017).
15. Mudelsee, M., Borngen, M., Tetzlaff, G. & Grunewald, U. No upward trends in the occurrence of extreme floods in central Europe. *Nature* **425**, 166–169 (2003).
16. Hartmann, D. L. et al. in *Climate Change 2013: The Physical Science Basis* (eds Stocker, T. F. et al.) Ch. 2 (IPCC, Cambridge Univ. Press, 2013).
17. Hirsch, R. M. & Archfield, S. A. Flood trends: not higher but more often. *Nat. Clim. Change* **5**, 198–199 (2015).
18. Sharma, A., Wasko, C. & Lettenmaier, D. P. If precipitation extremes are increasing, why aren't floods? *Water Resour. Res.* **54**, 8545–8551 (2018).
19. Wasko, C. Can temperature be used to inform changes to flood extremes with global warming? *Phil. Trans. R. Soc. A* **379**, 20190551 (2021).
20. Peterson, T. C. et al. Monitoring and understanding changes in heat waves, cold waves, floods, and droughts in the United States: state of knowledge. *Bull. Am. Meteorol. Soc.* **94**, 821–834 (2013).
21. Merz, R. & Blöschl, G. A process typology of regional floods. *Water Resour. Res.* <https://doi.org/10.1029/2002WR001952> (2003).
22. Sikorska, A. E., Viviroli, D. & Seibert, J. Flood-type classification in mountainous catchments using crisp and fuzzy decision trees. *Water Resour. Res.* **51**, 7959–7976 (2015).
23. Berghuijs, W. R., Woods, R. A., Hutton, C. J. & Sivapalan, M. Dominant flood generating mechanisms across the United States. *Geophys. Res. Lett.* **43**, 4382–4390 (2016).
24. Stein, L., Clark, M. P., Knoben, W. J., Pianosi, F. & Woods, R. A. How do climate and catchment attributes influence flood generating processes? A large-sample study for 671 catchments across the contiguous USA. *Water Resour. Res.* **57**, e2020WR028300 (2021).
25. Kemter, M., Merz, B., Marwan, N., Vorogushyn, S. & Blöschl, G. Joint trends in flood magnitudes and spatial extents across Europe. *Geophys. Res. Lett.* **47**, e2020GL087464 (2020).
26. Wang, G. et al. The peak structure and future changes of the relationships between extreme precipitation and temperature. *Nat. Clim. Change* **7**, 268–274 (2017).
27. Wasko, C., Sharma, A. & Lettenmaier, D. P. Increases in temperature do not translate to increased flooding. *Nat. Commun.* **10**, 5676 (2019).
28. Kapnick, S. & Hall, A. Causes of recent changes in western North American snowpack. *Clim. Dyn.* **38**, 1885–1899 (2012).
29. Wu, X., Che, T., Li, X., Wang, N. & Yang, X. Slower snowmelt in spring along with climate warming across the Northern Hemisphere. *Geophys. Res. Lett.* **45**, 12331–12339 (2018).
30. Arnell, N. W. & Gosling, S. N. The impacts of climate change on river flood risk at the global scale. *Clim. Change* **134**, 387–401 (2016).
31. Clow, D. W. Changes in the timing of snowmelt and streamflow in Colorado: a response to recent warming. *J. Clim.* **23**, 2293–2306 (2010).
32. De Michele, C. & Salvadori, G. On the derived flood frequency distribution: analytical formulation and the influence of antecedent soil moisture condition. *J. Hydrol.* **262**, 245–258 (2002).
33. Bennett, B., Leonard, M., Deng, Y. & Westra, S. An empirical investigation into the effect of antecedent precipitation on flood volume. *J. Hydrol.* **567**, 435–445 (2018).
34. Wasko, C. & Nathan, R. Influence of changes in rainfall and soil moisture on trends in flooding. *J. Hydrol.* **575**, 432–441 (2019).
35. Musselman, K. N. et al. Projected increases and shifts in rain-on-snow flood risk over western North America. *Nat. Clim. Change* **8**, 808–812 (2018).

Publisher's note Springer Nature remains neutral with regard to jurisdictional claims in published maps and institutional affiliations.

Springer Nature or its licensor (e.g. a society or other partner) holds exclusive rights to this article under a publishing agreement with the author(s) or other rightsholder(s); author self-archiving of the accepted manuscript version of this article is solely governed by the terms of such publishing agreement and applicable law.

© The Author(s), under exclusive licence to Springer Nature Limited 2022

Methods

Historical observations

Daily streamflow (Q) observations in 7,239 catchments (and their boundaries) across the globe (Supplementary Fig. 1) from 1950 to 2017 were obtained from a global streamflow collection^{36–41}, which consists of streamflow records from more than 20,000 catchments worldwide. The 7,239 catchments were chosen subject to the following selection criteria. First, the catchments should have daily Q records for at least 30 yr during 1950–2017. Second, the catchment areas are larger than 100 km² to encompass at least one grid cell of the meteorological datasets (at ~9 km spatial resolution) and smaller than 100,000 km². Third, the catchments should have a minimum impact from human interventions, including reservoir, urban afforestation/deforestation and water transfer. Thus, catchments with (1) reservoirs and dams whose reservoir capacity is larger than 10% of the mean annual Q (based on the Global Reservoir and Dam database v1.01)⁴², (2) urban areas larger than 5% (based on the GlobCover v2.3 map) and (3) areas with afforestation or deforestation larger than 10% (based on 30 m Landsat imagery from 2000 to 2013)⁴³, and (4) problematic water balance closure (that is, mean annual streamflow higher than mean annual precipitation, or the sum of mean annual streamflow and potential evapotranspiration lower than mean annual precipitation) are excluded.

Global hourly precipitation, volumetric soil water and 2 m air temperature from 1950–2017 were obtained from the ERA5-Land hourly dataset⁴⁴, with a spatial resolution of 0.1°. These gridded data were further upsampled to daily resolution and aggregated for individual catchments by averages and/or accumulations of the grids covered by the catchments. Snowmelt was estimated according to Hock's simple degree-day model⁴⁵ using daily precipitation and temperature data, with the temperature threshold and melt rate set at 274.5 K and 2 mm d⁻¹ K⁻¹ according to previous studies²³.

CMIP6 model simulations

We used outputs from 11 climate models participating in CMIP6⁴⁶ under historical forcing (1950–2014) and future emission scenarios (2015–2100; a high-emission scenario of SSP585 and a low-emission scenario of SSP245). The 11 CMIP6 models are MIROC-ESM2-0, MIROC6, GFDL-CM4, ACCESS-CM2, ACCESS-ESM1-5, INM-CM4-8, INM-CM5-0, IPSL-CM5A-LR, EC-Earth3, CMCC-CM2-SR5 and CMCC-ESM2. We used daily outputs of air temperature, precipitation and run-off. All outputs from the models were spatially resampled on a 1° × 1° grid using the first-order conservative remapping scheme⁴⁷. When comparing the modelled run-off with catchment observations, small catchments located close to each other may share the same grids, so we only used observations at catchments larger than 5,000 km² (857 catchments) for model validation.

Identification of flood events

The event identification method used in this study consists of four steps (Supplementary Fig. 2): (1) base flow separation, (2) identification of initial starts and ends of events, (3) refinement of the event starts and (4) estimation of the identification parameter. We used the one-parameter filter method⁴⁸ to separate base flow from daily streamflow. The recession constant of the method was quantified for each catchment using the Brutsaert-Nieber method⁴⁹ applied with the automatic base flow identification technique developed in ref.⁵⁰. We then identified individual flood events by locating their start- and endpoints. To achieve this, we first identified the local turning points (local peaks and valleys) of the hydrograph. The point with a higher (lower) flow than its preceding and following points was defined as the local peak (valley). The initial start-point was identified as the closest valley before the peak (peak of annual flow within a calendar year) when the total flow was initially higher than the base flow, while the end of an event was set at the first point on the falling limb of the hydrograph at which the quick flow fell below 10% of the peak

quick flow. Subsequently, we identified whether there was another potential start-point on the rising limb (from the initial start-point to the peak) that was also the endpoint of a small run-off event (for example, the event marked in blue in Supplementary Fig. 2c) preceding the objective flood event with annual peak flow (for example, the event marked in red in Supplementary Fig. 2c). This refined start-point should be located at the local valley where the quick flow was lower than a certain percentage (defined as the refinement threshold) of the maximum quick flow before it. Then, we compared the difference (quantified by standard deviation) in the run-off coefficients of flood events with and without small run-off events being removed. The value of the refinement threshold was determined on the basis of the assumption that a smaller difference in run-off coefficients of flood events would be achieved by removing small run-off events that should be treated as independent events with different run-off coefficients^{51,52}. Total daily rainfall during the rising period of the event (the period from the beginning of the event until the day when peak flow was observed) plus the rainfall-streamflow response period (time lag between rainfall and streamflow response⁵³) was used to estimate run-off coefficient for each event. For the regions with snowmelt, the sum of rainfall and snowmelt was calculated as the effective rainfall to identify flood events.

We further quantified event characteristics listed in Supplementary Table 1 for all the identified flood events (in total 246,170 events). These characteristics provide information on the rainfall, snowmelt and soil moisture dynamics preceding and during the flood events, which point to the triggers of events and were used as the indicators for the classification of flood types.

Classification of flood types

We classified the identified annual maximum flood events into four types, including: (1) IR-MF, occurring after short and high-intensity rainfall that rapidly fills the storage capacity or exceeds the infiltration capacity; (2) ES-MF, characterized by large amounts of rainfall over several days preceding the flood event and high antecedent soil moisture storage; (3) SM-MF, triggered by heavy snowmelt without (or with minor) rainfall; and (4) RS-MF, caused by high-intensity rainfall as well as slight snowmelt.

Hydrological classification of flood events based on hydrometeorological forcing within catchments (for example, rainfall and snowmelt) and catchment states (for example, soil moisture) is one of the most commonly used methods for flood typology⁵⁴. It can be further categorized into two approaches: the decision tree^{21,22,24,25} and the statistical clustering algorithm^{55,56}. In this study, we combined these two approaches to classify flood types by first constructing a decision tree to define the criteria for each flood type, this tree consisting of decision attributes and the attribute thresholds (Supplementary Fig. 4 and Table 1). The characteristics of each flood event were compared with the corresponding threshold values to decide which sub-group it belongs to. However, instead of predefining the thresholds subjectively, we first set the ranges of thresholds, that is, the 25th–75th percentile of the corresponding characteristics of all events (Supplementary Table 2). Then, we used a global optimization algorithm (SCE-UA)⁵⁷ to search for the optimal sets of thresholds with which the optimal clustering performance would be achieved. The clustering performance was evaluated by the Calinski-Harabasz index⁵⁸, a similarity index that quantifies the similarities within groups and the differences between groups, with a higher index representing better clustering performance. Combining the two approaches, the subjectivity of threshold determination could be minimized to some extent, and the built decision tree could help to better interpret classification results. A flowchart of the methodology used to categorize the flood events into four different types is illustrated in Supplementary Fig. 5. The resulting classification thresholds (one set of thresholds for all catchments) are provided in Supplementary Table 2.

Long-term trend analysis

We first created the long-term annual maximum precipitation and streamflow time series from available observations and CMIP6 models for the study period. We then estimated the linear trend of annual time series over the study period using the least squares fitting. A two-tailed Student's t -test was used to quantify the probability that the trend is statistically significantly different from zero. Trend analysis was performed for catchment/grid scale time series data and spatially aggregated time series data (that is, annual maximum precipitation and streamflow time series averaged across all catchments/grids or across the four groups of catchments/grids based on flood types).

Scaling relationship of precipitation and streamflow with temperature

The historical day-to-day sensitivities of precipitation and/or streamflow with temperature, defined as the scaling relationship, have been widely applied to project extreme precipitation and/or flooding for a future warmer climate^{6,7,26}. Taking the precipitation and temperature (P - T) scaling relationship as an example, we first stratified the daily precipitation of each catchment/grid within the analysis period according to the corresponding near-surface air temperature at the same catchment/grid in bins of equal width (a temperature bin size of 0.5 °C was used here). Then, a high-precipitation quantile (the 99th percentile) within each temperature bin was estimated to create a scaling curve that relates these estimated conditional quantiles to the average temperature of each bin (Supplementary Fig. 6). The peak point of the scaling curve was identified by applying the locally weighted scatterplot smoothing method⁵⁹. However, it should be noted that previous studies have also pointed out that the 'hook'-like structure (or peak structure) of the scaling curve might be rectified using sub-daily data⁶⁰. The same steps were implemented to obtain the scaling curves of streamflow with temperature.

To explore changes in the scaling relationships of precipitation and streamflow with temperature under future warming, we investigated the shift in scaling curves between epochs, where one epoch (the period 2015–2100 under SSP585/SSP245 scenario) was warmer than the other (the 1950–2014 period under historical forcing). Referring to the method applied in ref.²⁶, the shift rate (α_p , % °C⁻¹) was quantified by the change in the peak points of the two scaling curves (Supplementary Fig. 6b) using the following equation:

$$\alpha_p = \left(e^{\frac{\ln(p_{\text{peak}}^2) - \ln(p_{\text{peak}}^1)}{T_{\text{peak}-p}^2 - T_{\text{peak}-p}^1}} \right) \times 100 \quad (1)$$

where $T_{\text{peak}-p}^1$ and $T_{\text{peak}-p}^2$ represent the temperature at which the precipitation percentile in the scaling curve reaches the peak, p_{peak}^1 and p_{peak}^2 under historical and future climates, respectively. The same method was used to quantify the shift rate of the Q - T scaling curves under warming (Supplementary Fig. 6d).

Data availability

The streamflow records were obtained from the Global Runoff Data Centre (<http://www.bafg.de/GRDC>), the United States Geological Survey GAGES-II database (<https://www.sciencebase.gov>), the Water Survey of Canada Hydrometric Data (HYDAT; <https://www.canada.ca/en/environment-climate-change>), the Catchment Characterisation and Modelling–Joint Research Centre database (<https://ccm.jrc.ec.europa.eu/>), the HidroWeb portal of the Brazilian Agência Nacional de Águas (<http://www.snirh.gov.br/hidroweb>), the Australian Bureau of Meteorology (<http://www.bom.gov.au/water-data>) and the Chilean Center for Climate and Resilience Research (<http://www.cr2.cl/datos-de-caudales/>). The Global Reservoir and Dam database is available at <https://sedac.ciesin.columbia.edu/data/set/grand-v1-dams-rev01>. The GlobCover v2.3 map is available

at http://due.esrin.esa.int/page_globcover.php. The Global forest change dataset is available at <http://earthenginepartners.appspot.com/science-2013-global-forest>. The ERA5-Land dataset is available at <https://www.ecmwf.int/en/era5-land>. The CMIP6 data can be accessed through the Earth System Grid Federation (ESGF) system (<https://esgf-node.llnl.gov/search/cmip6/>).

Code availability

The code⁶¹ used as the basis for this study is available at <https://doi.org/10.5281/zenodo.7319421>.

References

36. Beck, H. E. et al. Bias correction of global high-resolution precipitation climatologies using streamflow observations from 9372 catchments. *J. Clim.* **33**, 1299–1315 (2020).
37. Lehner, B. *Derivation of Watershed Boundaries for GRDC Gauging Stations Based on the Hydrosheds Drainage Network* Tech. Rep. 41 (Global Runoff Data Centre in the Federal Institute of Hydrology (BfG), Germany, 2012).
38. Falcone, J. A., Carlisle, D. M., Wolock, D. M. & Meador, M. R. GAGES: a stream gage database for evaluating natural and altered flow conditions in the conterminous United States. *Ecology* **91**, 621 (2010).
39. Vogt, J. V., Soille, P., Colombo, R., Paracchini, M. L. & de Jager, A. *Digital Terrain Modelling: A Pan-European River and Catchment Database* (European Communities, Italy, 2007).
40. Zhang, Y. et al. *Collation of Australian Modeller's Streamflow Dataset for 780 Unregulated Australian Catchments* Water for a Healthy Country Flagship Report (CSIRO, 2013).
41. Alvarez-Garretón, C. et al. The CAMELS-CL dataset: catchment attributes and meteorology for large sample studies – Chile dataset. *Hydrol. Earth Syst. Sci.* **22**, 5817–5846 (2018).
42. Lehner, B. et al. High-resolution mapping of the world's reservoirs and dams for sustainable river-flow management. *Front. Ecol. Environ.* **9**, 494–502 (2011).
43. Hansen, M. C. et al. High-resolution global maps of 21st-century forest cover change. *Science* **342**, 850–853 (2013).
44. Muñoz-Sabater, J. et al. ERA5-Land: a state-of-the-art global reanalysis dataset for land applications. *Earth Syst. Sci. Data* **13**, 4349–4383 (2021).
45. Hock, R. Temperature index melt modelling in mountain areas. *J. Hydrol.* **282**, 104–115 (2003).
46. Eyring, V. et al. Overview of the Coupled Model Intercomparison Project Phase 6 (CMIP6) experimental design and organization. *Geosci. Model Dev.* **9**, 1937–1958 (2016).
47. Jones, P. W. First- and second-order conservative remapping schemes for grids in spherical coordinates. *Mon. Weather Rev.* **127**, 2204–2210 (1999).
48. Lyne, V. & Hollick, M. Stochastic time-variable rainfall-runoff modelling. In *Institute of Engineers Australia National Conference* (ed. Ratcliffe, J. S.) 89–93 (Barton, Australia: Institute of Engineers, 1979).
49. Brutsaert, W. & Nieber, J. L. Regionalized drought flow hydrographs from a mature glaciated plateau. *Water Resour. Res.* **13**, 637–643 (1977).
50. Cheng, L., Zhang, L. & Brutsaert, W. Automated selection of pure base flows from regular daily streamflow data: objective algorithm. *J. Hydrol. Eng.* **21**, 06016008 (2016).
51. Tarasova, L., Basso, S., Zink, M. & Merz, R. Exploring controls on rainfall-runoff events: 1. Time series-based event separation and temporal dynamics of event runoff response in Germany. *Water Resour. Res.* **54**, 7711–7732 (2018).
52. Tarasova, L. et al. A process-based framework to characterize and classify runoff events: the event typology of Germany. *Water Resour. Res.* **56**, e2019WR026951 (2020).

53. Giani, G., Rico-Ramirez, M. A. & Woods, R. A. A practical, objective, and robust technique to directly estimate catchment response time. *Water Resour. Res.* **57**, e2020WR028201 (2021).
54. Tarasova, L. et al. Causative classification of river flood events. *Wiley Interdiscip. Rev. Water* **6**, e1353 (2019).
55. Tarasova, L., Basso, S., Poncelet, C. & Merz, R. Exploring controls on rainfall-runoff events: 2. Regional patterns and spatial controls of event characteristics in Germany. *Water Resour. Res.* **54**, 7688–7710 (2018).
56. Turkington, T., Breinl, K., Ettema, J., Alkema, D. & Jetten, V. A new flood type classification method for use in climate change impact studies. *Weather Clim. Extrem.* **14**, 1–16 (2016).
57. Duan, Q., Sorooshian, S. & Gupta, V. K. Optimal use of the SCE-UA global optimization method for calibrating watershed models. *J. Hydrol.* **158**, 265–284 (1994).
58. Caliński, T. & Harabasz, J. A dendrite method for cluster analysis. *Commun. Stat.* **3**, 1–27 (1974).
59. Cleveland, W. S. Robust locally weighted regression and smoothing scatterplots. *J. Am. Stat. Assoc.* **74**, 829–836 (1979).
60. Visser, J. B., Wasko, C., Sharma, A. & Nathan, R. Eliminating the ‘hook’ in precipitation–temperature scaling. *J. Clim.* **34**, 9535–9549 (2021).
61. Zhang, S. Code for “Reconciling disagreement on global river flood changes in a warming climate”. *Zenodo* <https://doi.org/10.5281/zenodo.7319421> (2022).

Acknowledgements

This study was supported by the National Natural Science Foundation of China under grant agreement numbers 42088101 (S. Zhang and Y.D.) and 42175168 (S. Zhang) and the Innovation Group Project of Southern Marine Science and Engineering Guangdong Laboratory

(Zhuhai) under grant agreement number 311021009 (S. Zhang, Y.D. and Z.W.). L. Zhou acknowledges the US National Science Foundation (NSF AGS-1952745 and AGS-1854486).

Author contributions

S. Zhang, Y.D. and L. Zhou designed the study. S. Zhang, Y.Y. and Z.W. collected the data. S. Zhang performed the analysis. All authors contributed to the interpretation of the results. S. Zhang wrote the initial manuscript with contributions from L. Zhou, L. Zhang, S. Zhou and Y.Y. All authors reviewed and approved the manuscript.

Competing interests

The authors declare no competing interests.

Additional information

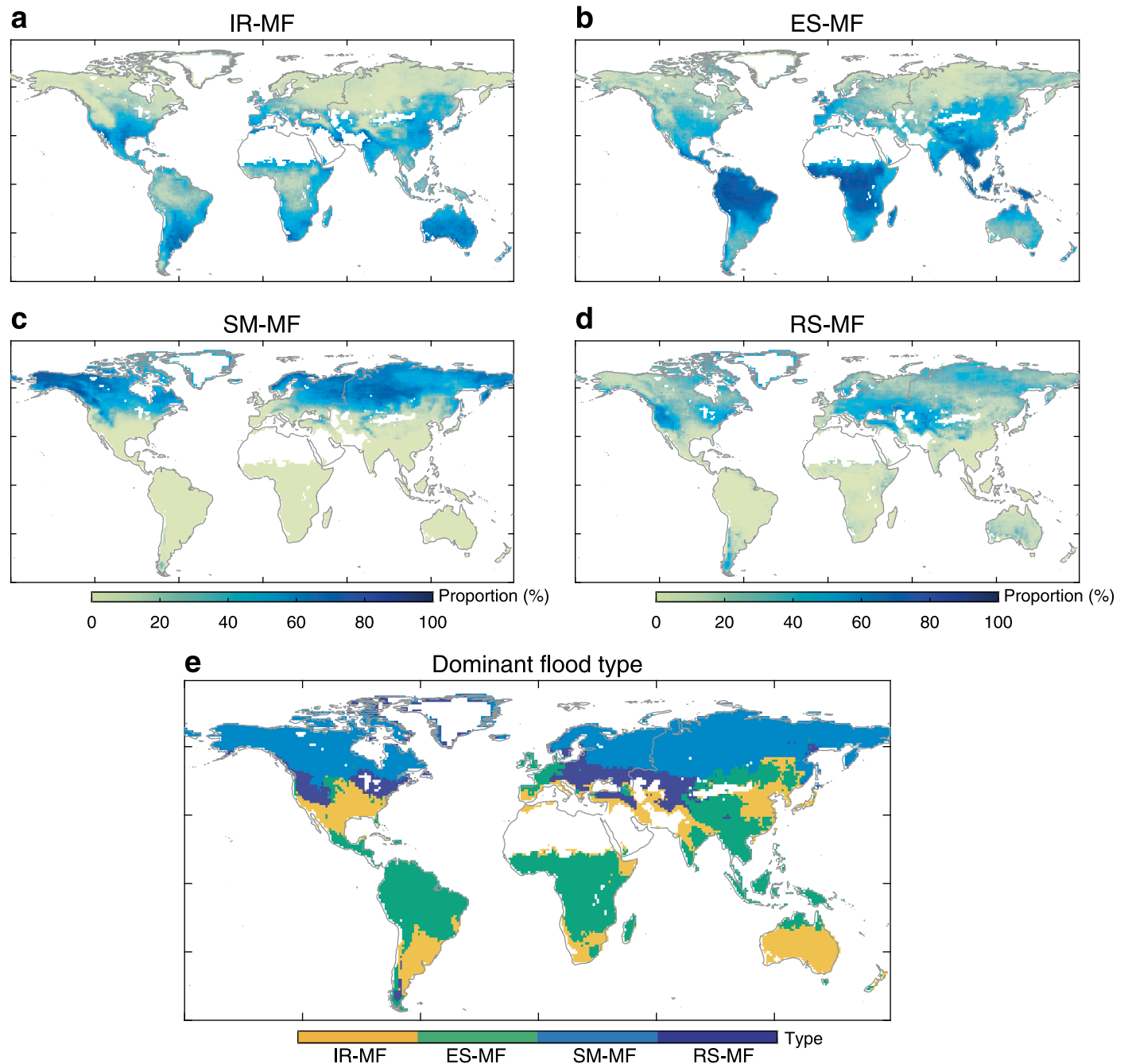
Extended data is available for this paper at <https://doi.org/10.1038/s41558-022-01539-7>.

Supplementary information The online version contains supplementary material available at <https://doi.org/10.1038/s41558-022-01539-7>.

Correspondence and requests for materials should be addressed to Shulei Zhang or Yongjiu Dai.

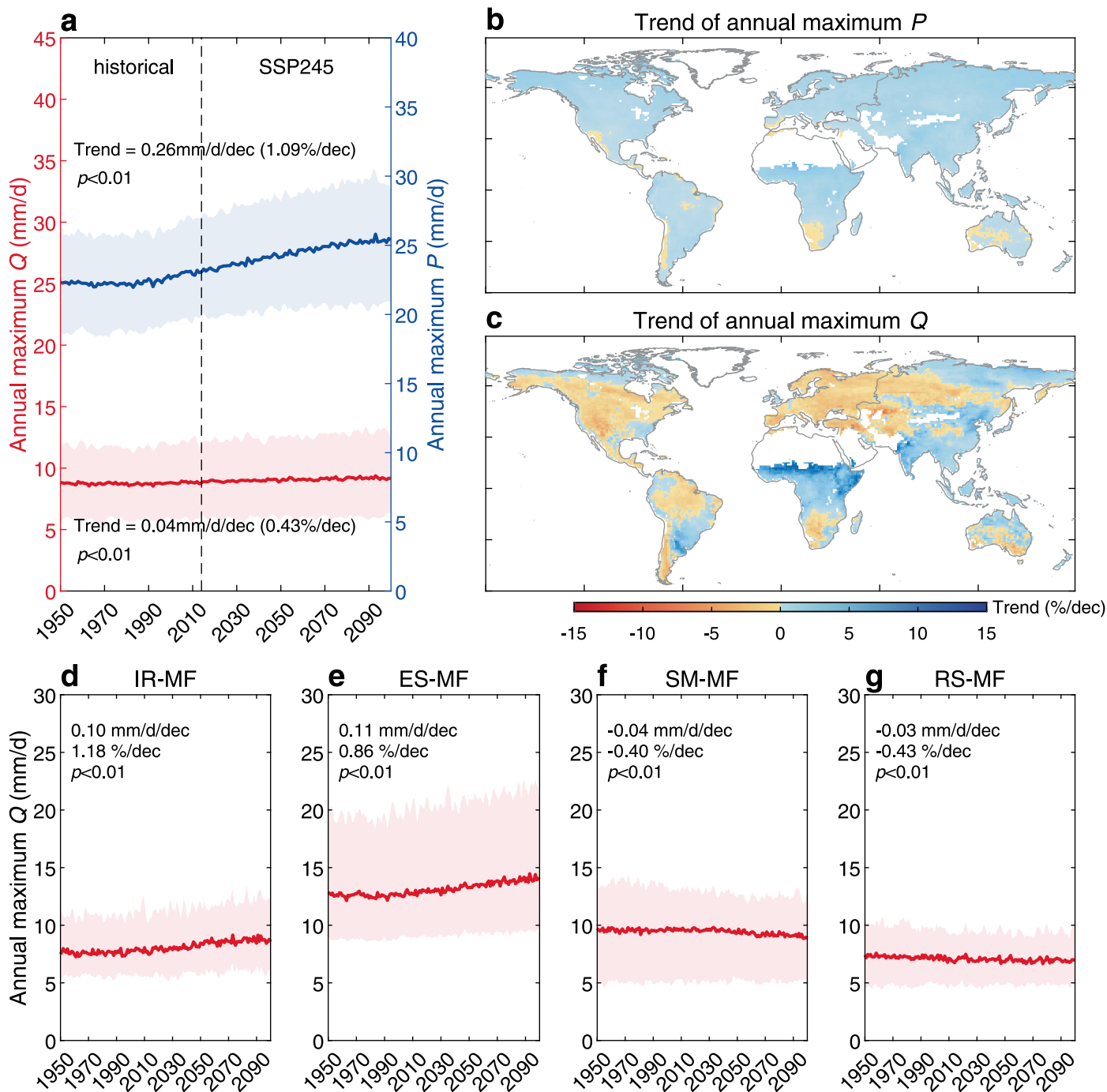
Peer review information *Nature Climate Change* thanks Larisa Tarasova and the other, anonymous, reviewer(s) for their contribution to the peer review of this work.

Reprints and permissions information is available at www.nature.com/reprints.



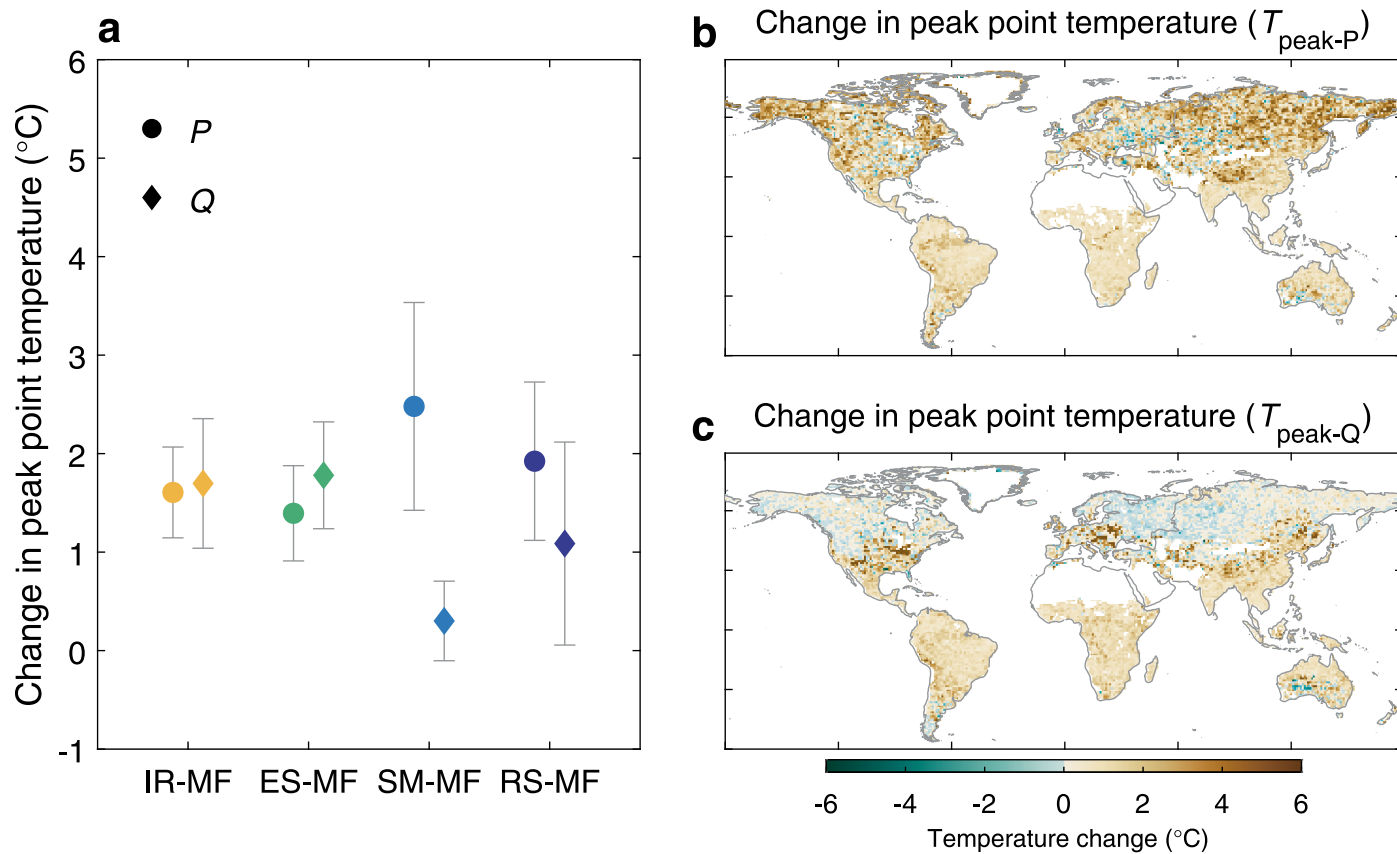
Extended Data Fig. 1 | Global classifications of annual maximum flood events based on CMIP6 outputs. a-d. Global proportions of four flood types, IR-MF (a), ES-MF (b), SM-MF (c), and RS-MF (d), based on the ensemble mean of classification outcomes for individual CMIP6 models using outputs from 1950 to

2014 under historical forcing. **e.** Regions dominated by different types of floods (that is, the flood type showing the highest proportion of occurrence for each region).



Extended Data Fig. 2 | Changes in flood and extreme precipitation from the historical to the future period (SSP245 scenario). **a**, Time series of annual maximum precipitation (P) and streamflow (Q) averaged over the global land area from the historical (1950–2014 under historical forcing) to the future (2015–2100 under SSP245 scenario) period based on the outputs of 11 CMIP6 models. Shaded bands represent the variation by individual models. The trends were estimated based on the ensemble mean of model outputs using linear

regression with significance level (a two-tailed student's t test) labeled in the panel. **b–c**, Global patterns of the trends of annual maximum P (**b**) and Q (**c**) from 1950 to 2100. The whitespace represents the dry lands with very limited runoff. **d–g**, Time series of annual maximum Q averaged over regions dominated by different flood types, IR-MF (**d**), ES-MF (**e**), SM-MF (**f**), and RS-MF (**g**). The shaded bands, solid lines and dotted lines are similarly defined as those in panel **a**.



Extended Data Fig. 3 | Changes in peak point temperatures of the P - T and Q - T scaling curves from the historical to the future period (SSP585 scenario). **a**, Comparison between the changes in peak point temperatures of the P - T and Q - T scaling curves ($T_{\text{peak-P}}$ and $T_{\text{peak-Q}}$) averaged over regions dominated by different flood types based on the outputs of 11 CMIP6 models from the historical

(1950-2014 under historical forcing) to the future (2015-2100 under SSP585 scenario) period. Error bars indicate the variations among 11 models (mean value \pm one standard deviation). **b-c**, Global spatial patterns of the changes in $T_{\text{peak-P}}$ (**b**) and $T_{\text{peak-Q}}$ (**c**) from the historical to the future period.